Applied Catalysis B: Environmental 200 (2017) 150–163

Contents lists available at ScienceDirect

Applied Catalysis B: Environmental

journal homepage: www.elsevier.com/locate/apcatb

Study of the decomposition and detoxification of the herbicide bentazon by heterogeneous photocatalysis: Kinetics, intermediates and transformation pathways

Chrysanthi Berberidou[a,1], Vasiliki Kitsiou[a,1], Eleutheria Kazala[a], Dimitra A. Lambropoulou[a], Athanasios Kouras[a], Christina I. Kosma[b], Triantafyllos A. Albanis[b], Ioannis Poulios[a,*]

[a] Department of Chemistry, Aristotle University of Thessaloniki, 54124 Thessaloniki, Greece
[b] Department of Chemistry, University of Ioannina, 45110 Ioannina, Greece

ARTICLE INFO

Article history:
Received 18 April 2016
Received in revised form 24 June 2016
Accepted 27 June 2016
Available online 28 June 2016

Keywords:
Bentazon
Pesticide
Photocatalytic
Toxicity
Intermediates

ABSTRACT

Photocatalytic degradation and mineralization of the herbicide bentazon in aqueous solutions has been investigated. The pseudo-first order degradation kinetics was studied under different operational conditions, such as type of photocatalyst, catalyst loading, initial pH and addition of electron acceptors. The degradation rates proved to be strongly influenced by these parameters. Organic sulfur and nitrogen were only partially converted into inorganic in the presence of TiO_2 P25 or TiO_2 Kronos vlp 7000 and UV-A. The presence of H_2O_2 led to either enhancement or decrease of the initial degradation rates, depending on the type of catalyst employed. Intermediate products formed during photocatalytic treatment were identified by means of a high resolution LIT Orbitrap LC-ESI/MS system. 21 intermediates including dimers, hydroxy and/or keto bentazon derivatives, and further oxidized species were identified and detailed transformation pathways have been proposed. Acute toxicity profiles using marine bacteria *Vibrio fischeri* showed an increasing trend at the first stages of oxidation, implying the progressive formation of intermediates more toxic than the parent molecule, or synergistic effects among the transformation products. Thereafter, ecotoxicity was completely eliminated within 90 min of irradiation under the investigated conditions. Phytotoxicity tests, carried out on the monocotyl *Sorghum saccharatum* and the dicotyls *Sinapis alba* and *Lepidium sativum*, showed similar responses of the three plant species to the photocatalytically treated samples, resulting to complete removal of phytotoxicity under the employed conditions.

1. Introduction

Modern agriculture is supported by the use of pesticides to control a variety of pests that can damage crops and livestock and reduce productivity. However, the active substances contained in pesticides are often toxic for living organisms, resistant to degradation, while they disturb the natural balance of ecosystems. Moreover, they constitute a risk for water quality in agricultural areas due to the fact that their components may migrate through soil and subsoil and pollute both surface waters and groundwater [1]. Many studies have established the epidemiological association between pesticide exposure and elevated rate of chronic diseases in humans, including diabetes, neurodegenerative disorders like Parkinson, Alzheimer and amyotrophic lateral sclerosis (ALS) [2], while numerous pesticides are characterized as endocrine disruptors, interfering with hormone regulation causing, among others, birth defects and cancer [3,4].

Bentazon (3-isopropyl-1H-2,1,3-benzothiadiazin-4(3H)-one 2,2-dioxide) is a selective herbicide for weed control in soybeans, cereals and rice, generally used as a post-emergence herbicide. It is categorized under the thiadiazine group of chemicals and acts by interfering with photosynthesis. It is applied primarily as direct foliar spray [5]. Abernathy and Wax [6] found that bentazon exhibits high mobility in soil at neutral pH, due to its high water solubility and strong anionic characteristics [7]. Since bentazon does not attach to soil particles, it probably moves easily through soil in ground water, posing problems for several resources,

* Corresponding author.
E-mail address: poulios@chem.auth.gr (I. Poulios).
[1] Equally contributing authors.

http://dx.doi.org/10.1016/j.apcatb.2016.06.068
0926-3373/

including drinking water [8,9]. World Health Organization (WHO) classifies this pesticide as moderately hazardous (class II) and proposes 30 $\mu g\,L^{-1}$ as the maximum acceptable concentration of bentazon in drinking water [10,11]. Toxicological studies show that this herbicide is toxic to certain fish and bird species and moderately toxic in mammals after oral or dermal exposure [3,12]. Bentazon exhibits acute and chronic toxicity in humans, while deaths have been reported after ingestion of high doses [13,14].

Thus, the monitoring of such xenobiotics in the aquatic environment is progressively becoming a priority for government agencies, regulatory agencies and the general public. However, the wide range of pesticides in use makes research extremely difficult for providing a single method for the effective removal of pesticides that applies universally [15]. In view of this, the development of sustainable technologies that can promote the degradation of such bio-recalcitrant organic compounds is necessary. A promising way to achieve purification of water and wastewater contaminated with pesticides is the exploitation of advanced oxidation processes (AOPs) [16].

Among the different technologies proposed as AOPs, heterogeneous photocatalysis is an efficient technique used to degrade a variety of toxic agrochemical substances including pesticides, in the presence of artificial or solar light [17–19]. Photocatalytic degradation and mineralization of bentazon has been previously reported [20,21]. Our present paper provides data concerning heterogeneous photocatalytic oxidation of bentazon, in terms of degradation, mineralization and ecotoxicity. Furthermore, employing a linear ion trap (LIT) Orbitrap LC-ESI/MS high resolution system, 21 transformation products (TPs) including dimers, hydroxy and/or keto bentazon derivatives and further oxidized species have been identified. To the best of our knowledge, this is the first report in which such a great number of intermediates has been detected and described in such structural details during the oxidation of bentazon by an AOP and thus, new possible degradation pathways are proposed. Finally, for the first time we provide data concerning the reduction of phytotoxicity of bentazon in aqueous solutions subjected to TiO_2 mediated photocatalysis, employing three species of eukaryotic plants. This study is implemented within the framework of a research project aiming to the development of a combined system for the detoxification and reuse of wastewater containing pesticides by solar photocatalysis and constructed wetlands.

2. Materials and methods

2.1. Materials

Bentazon (3-isopropyl-1H-2,1,3-benzothiadiazin-4(3H)-one 2,2-dioxide, CAS No. 25057-89-0, M_r: 240.28 g mol^{-1}, Product No: 32052, Pestanal, analytical standard) was a product of Fluka (Sigma-Aldrich Laborchemicalien GmbH) and was used as received.

The catalysts used were TiO_2 P25 (Degussa Evonik GmbH, anatase/rutile = 3.6/1, BET: 50 $m^2\,g^{-1}$, nonporous), TiO_2 UV-100 (Hombikat, 100% anatase, BET: 300 $m^2\,g^{-1}$), TiO_2 Kronos vlp 7000, Kronos Worldwide, Inc., 100% anatase, BET: 250 $m^2\,g^{-1}$, carbon-doped and ZnO (Merck, BET: 10 $m^2\,g^{-1}$). All other reagent-grade chemicals were purchased from Merck and were used without further purification. Doubly distilled water was used throughout the study.

2.2. Photocatalytic experiments

Experiments were performed in a closed Pyrex cell of 600 mL capacity, at a working volume of 500 mL, fitted with a central 9 W lamp, under magnetic stirring and constant temperature (25 ± 0.1 °C), as previously described [22]. The incident photon flow of the UV-A (Osram Dulux S, 9W/78, maximum emission: 365 nm) and visible (Osram Dulux S, 9W/71, maximum emission: 450 nm) irradiation sources, determined by chemical actinometry using potassium ferrioxalate [23], was 97×10^{-6} and 78×10^{-6} Einstein $L^{-1}\,min^{-1}$, respectively.

2.3. Analytical procedures

Changes in the concentration of bentazon were monitored via its characteristic absorption band at 333 nm using a UV–vis spectrophotometer (UV-1700, PharmaSpec, Shimadzu), since a linear dependence between the initial concentration of the herbicide and the absorption at 333 nm is observed.

Determination of dissolved organic carbon (DOC) was conducted according to standard methods by a total organic carbon (TOC) analyser (Shimandzu V_{CSH} 5000).

Inorganic ions were determined in a Shimadzu system consisted of an LC-10 AD pump, a CDD-6A conductometric detector (0.25 μL flow-cell) and a CTO-10A column oven. Cations were separated on an Alltech Universal column (100 mm × 4.6 mm) preceded by a guard column (7.5 mm × 4.6 mm) of the same material using 3 mM methanesulfonic acid at 1.5 mL min^{-1} constant flow. Anions were separated on an Alltech Allsep column (100 mm × 4.6 mm) preceded by a guard column (7.5 mm × 4.6 mm) of the same material using a phthalic acid and lithium hydroxide mixture of 4 mM (pH 4.00) at 1.5 mL min^{-1} constant flow. Column and conductivity cell temperatures were held constant at 35 °C and 38 °C, respectively. Mobile phases were degassed with helium stream before LC analysis. Calibration curves (0.01–10 mg L^{-1}) were constructed for each ion. The method detection limits were 0.03 mg L^{-1} for NH_4^+ and 0.03, 0.07, 0.06 mg L^{-1} for NO_3^-, SO_4^{2-} and Cl^-, respectively.

Some photocatalytic experiments were repeated three times to check the reproducibility of the experimental results. The accuracy of the optical density values was within ±5%, while the respective one of DOC and inorganic ions analysis was ±10%.

Bentazon and its TPs were determined by a Shimadzu liquid chromatograph with a photodiode array (PDA) detector coupled in series with a mass spectroscopy (MS) detector (LCMS-2010 EV) equipped with an atmospheric pressure electrospray ionization source (ESI). The HPLC system consisted of a SIL 20A autosampler with the volume injection set to 10 μL and a LC-20 AB pump both from Shimadzu (Kyoto, Japan). The column used was a CNW HPLC Athena C18 column, 4.6 mm × 250 mm and 5 μm pore size. The mobile phase was H_2O-HCOOH 0.1% (A) and MeOH-HCOOH 0.1% (B) with a flow rate of 0.4 mL min^{-1}. For bentazon determination, a linear gradient elution starting with 30% (A) in (B) and reaching 0% (A) in (B) within 8 min was followed. MS measurements were carried out in negative ionisation (NI) mode and selected ion monitoring (SIM) acquisition at 239 *m/z*. A longer gradient program was followed for TPs analysis by using the same mobile phase (0 min 10% B, 1.0 min 10% B, 4 min 40% B, 50 min 90% B, 52 min 90% B, 52.1 min 10% B).

The TPs generated during photocatalytic oxidation of bentazon were further characterized by a high resolution MS system (UPLC-ESI/MS system) in negative ionization mode. The LC system was equipped with an Accela Autosampler, an Accela LC pump and a linear ion trap (LIT) Orbitrap mass spectrometer (Thermo Fisher Scientific, Germany). The chromatographic separation of the compounds was conducted using a Hypersil Gold column (150 mm × 2.1 mm, Thermo Fisher Scientific, San Jose, USA), at 30 °C. Injection volume was 10 μL and flow rate was adjusted at 200 μL min^{-1}. Gradient mobile phase composition was adopted using water/5 mM formic acid as solvent A and methanol/5 mM formic acid as solvent B with the following program: 0 min 10% B, 1.0 min 10% B, 4 min 40% B, 15 min 60% B, 17 min 90% B, 17.1 min 10% B.

2.4. Ecotoxicity analysis

Ecotoxicity evaluation based on the bioluminescence measurements of marine bacteria *Vibrio fischeri* (*V. fischeri*) was applied to provide information on acute toxicity of the TPs formed during photocatalysis. The osmolality of the samples was adjusted by 2% w/v NaCl, while pH was adjusted between 6.5–8.5. Toxicity was evaluated using the Microtox Model 500 Analyzer (Azur Environmental). Freeze-dried bacteria, reconstitution solution, diluent (2% w/v NaCl) and adjustment solution (non-toxic, 22% w/v NaCl) were obtained from Azur. Samples were tested in a medium containing 2% w/v NaCl, in five dilutions and luminescence was recorded after 5, 15 and 30 min of incubation. The inhibition of bioluminescence, compared with a toxic-free control to give the percentage of inhibition, was calculated using the Microtox calculation software.

2.5. Phytotoxicity evaluation

Phytotoxicity measurements of bentazon subjected to photocatalytic treatment were carried out using the standard Phytotoxkit microbiotest, a bioassay based on three species of higher plants: the monocotyl *Sorghum saccharatum* (*S. saccharatum*) and the dicotyls garden cress *Lepidium sativum* (*L. sativum*) and mustard *Sinapis alba* (*S. alba*). This assay measures both the decrease/absence of seed germination and the decrease of root growth after 3 days of exposure of the seeds to the sample. For this purpose, 90 cm^3 of reference soil were added in the lower compartment of a test plate and hydrated with 35 mL of the sample. A control test was performed using identical volumes of distilled water. The soil surface was flatten and covered by paper filter. Tests were carried out in three replicates for each sample and for each type of plant. Prepared Phytotoxkit plates were incubated at 25 °C for 3 days. Digital pictures of the plates were analyzed using ImageJ v1.49 software (Wayne Rasband, National Institutes of Health, USA). Average values were used for final calculation of the percentage inhibition of root growth, according to the following equation:

$$\frac{A-B}{A} \times 100 = \text{inhibition}\,(\%) \quad (1)$$

where A represents mean root length in distilled water and B the mean root length in the test sample.

3. Results and discussion

3.1. Screening of catalysts

Results of the photodegradation of a 20 mg L^{-1} bentazon solution containing 0.5 g L^{-1} ZnO, TiO_2 P25, TiO_2 UV-100 or TiO_2 Kronos vlp 7000 are shown in Fig. 1, while the respective initial degradation rates, r_0, are presented in Table 1. The amount of the organic molecule present in the aqueous suspension is plotted as a function of the irradiation time. Under the given experimental conditions, ZnO and TiO_2 P25 appear to be the best catalysts, resulting after 90 min of UV-A illumination to 97 and 81% degradation of the pesticide, respectively. Although ZnO has similar band gap energy and band edge positions to TiO_2, its non-stoichiometry leads to electron mobility of at least two orders of magnitude higher than TiO_2. This results in a quicker charge transfer with the various species in solution and consequently, to lower recombination rates in comparison to TiO_2 [24,25]. However, even though ZnO exhibited the highest catalytic efficiency under the studied conditions, its application in photocatalysis is limited due to corrosion and photocorrosion phenomena [26,27]. At pH values below 9.0 ZnO dissolution takes place, which increases by illumination, as a result of the attack of the photogenerated holes on the Zn—O bonds [26]. This leads to a release of Zn^{2+} into the suspension, increasing toxicity, taking into account that for *V. fischeri* the EC_{50} for Zn^{2+} is 1.62 mg L^{-1} [17,28].

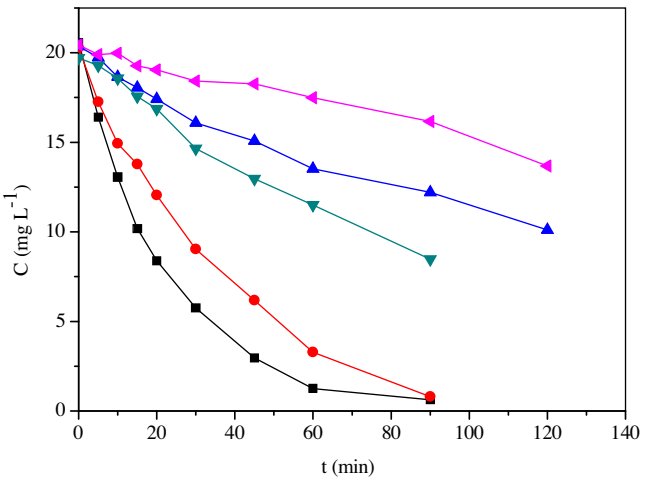

Fig. 1. Photocatalytic degradation of 20 mg L^{-1} of bentazon in the presence of various commercial catalysts at an initial concentration of 0.5 g L^{-1} and UV-A irradiation: (■) ZnO, (●) TiO_2 P25, (▼) TiO_2 Kronos vlp 7000, (▲) TiO_2 UV-100, (◄) TiO_2 Kronos vlp 7000 and visible irradiation.

Table 1
Initial rates of photodegradation (r_0) of 20 mg L^{-1} bentazon in the presence of 0.5 g L^{-1} of various photocatalysts.

Conditions	r_0 (mg L^{-1} min^{-1})
0.5 g L^{-1} ZnO	0.754 ± 0.049
0.5 g L^{-1} ZnO, 100 mg L^{-1} H_2O_2	0.341 ± 0.008
0.5 g L^{-1} TiO_2 P25	0.536 ± 0.040
0.5 g L^{-1} TiO_2 P25, 100 mg L^{-1} H_2O_2	1.096 ± 0.112
0.5 g L^{-1} TiO_2 P25, 7 mg L^{-1} Fe^{3+}	0.777 ± 0.224
0.5 g L^{-1} TiO_2 Kronos vlp 7000	0.171 ± 0.011
0.5 g L^{-1} TiO_2 Kronos vlp 7000, 100 mg L^{-1} H_2O_2	0.054 ± 0.003
0.5 g L^{-1} TiO_2 Kronos vlp 7000, 7 mg L^{-1} Fe^{3+}	0.198 ± 0.012
0.5 g L^{-1} TiO_2 Kronos vlp 7000, visible	0.065 ± 0.004
0.5 g L^{-1} TiO_2 UV-100	0.144 ± 0.006
0.5 g L^{-1} TiO_2 UV-100, 100 mg L^{-1} H_2O_2	0.026 ± 0.003
0.5 g L^{-1} TiO_2 UV-100, 7 mg L^{-1} Fe^{3+}	0.730 ± 0.135
100 mg L^{-1} H_2O_2	0.012 ± 0.002
7 mg L^{-1} Fe^{3+}	0.166 ± 0.067

On the other hand, the efficiency of TiO_2 UV-100 and TiO_2 Kronos vlp 7000 in the oxidation of bentazon under UV-A irradiation, is a considerably slower process in comparison to TiO_2 P25, resulting to 50 and 33% degradation, respectively, after 120 min of illumination (Fig. 1). The superiority of TiO_2 P25 in comparison to the other two commercial catalysts, may be attributed to the morphology of its crystallites, which has been proposed as one of the most critical properties for its high photocatalytic efficiency. In the case of TiO_2 P25, a transfer of the photogenerated electrons from rutile to anatase particles takes place, leading to stabilization of charge separation and thus, limiting recombination of the photogenerated carriers [29]. Additionally, the small size of rutile particles in this formulation and their close proximity to anatase particles are crucial to enhance catalytic activity. The higher efficiency of TiO_2 P25 in comparison to TiO_2 Kronos vlp 7000 under UV-A has also been reported in previous studies [30,31].

Furthermore, TiO_2 Kronos vlp 7000 under visible irradiation resulted to the lowest degradation rates of bentazon (Fig. 1 and Table 1). This photocatalyst, according to the manufacturer, is carbon-doped and is, therefore, expected to absorb also part of the visible light spectrum ($\lambda \geq 400$ nm). C-doping involves substitution of oxygen by carbon atoms producing new energy states deep in the TiO_2 band gap, responsible for visible light absorption [32]. The low photocatalytic efficiency of TiO_2 Kronos vlp 7000

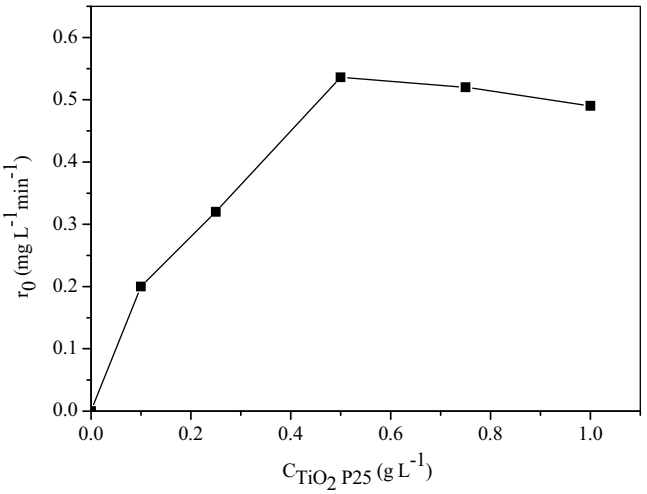

Fig. 2. Effect of TiO_2 P25 concentration on initial degradation rate (r_0) of 20 mg L^{-1} bentazon, during photocatalytic oxidation under UV-A irradiation.

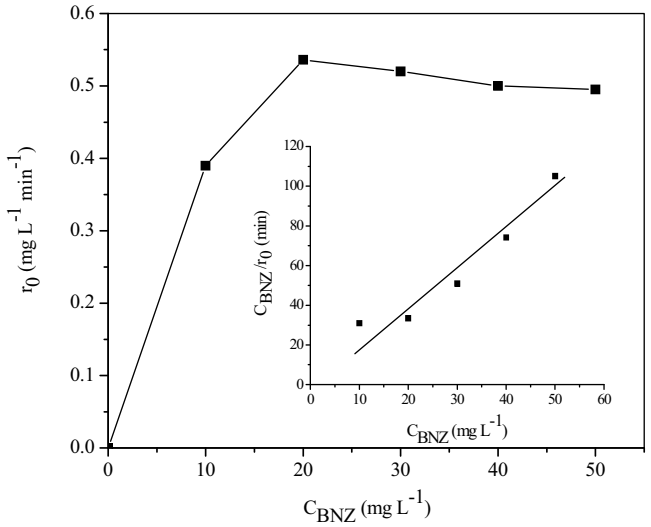

Fig. 3. Plot of r_0 vs. C_{eq} at various initial concentrations of bentazon from 10 to 50 mg L^{-1} for constant concentration of TiO_2 P25 at 0.5 g L^{-1}. Inset: Linear transformation of C_{eq}/r_0 vs. C_{eq} according to Eq. (3).

under visible irradiation in comparison to UV-A may be attributed to different degradation mechanisms followed in each case. While oxidation mediated by undoped TiO_2 in the presence of UV-A is associated with the production of $OH^{\bullet}$, the direct formation of $OH^{\bullet}$ from h^+ during photocatalysis with doped TiO_2 materials is thermodynamically implausible because of the position of the valence band [33,34]. Fotiou et al. recently demonstrated that the main reactive oxygen species in the case of photocatalytic degradation of cyanotoxins employing TiO_2 Kronos vlp 7000 under visible light is superoxide ($O_2^{\bullet -}$) and that $OH^{\bullet}$ and $^1O_2$ do not have an important role in the process [31].

3.2. Effect of catalyst's loading

TiO_2 dosage in slurry photocatalytic processes is an important factor that can strongly influence degradation of the organic compound. The values of the initial degradation rate in relation to the catalyst dose follow a Langmuir type isotherm, suggesting that r_0 might reach a saturation value at higher TiO_2 concentrations (Fig. 2) [35]. In this study, the optimum value for TiO_2 P25 is 0.5 g L^{-1}, while further increase in the amount of P25 leads to a slight decrease in the efficiency of photodegradation (Fig. 2). This limit depends on the nature of the organic compound, on the geometry and the working conditions of the reactor and corresponds to the optimum of light absorption. Above this optimum concentration, the catalyst's particles hinder penetration of UV-A irradiation and increase light scattering, while other phenomena like agglomeration (particle-particle interactions) may result in a loss of surface area, available for light-harvesting [36].

3.3. Effect of bentazon's concentration

The effect of the initial concentration of bentazon on the initial reaction rate of photodecomposition, in the presence of TiO_2 P25, is shown in Fig. 3. The r_o values were independently obtained by a linear fit of the C-t data in the range of 10–50 mg L^{-1} of initial bentazon concentration. The curve is reminiscent of a Langmuir type isotherm for which the rate of photodecomposition increases sharply, displaying afterwards a slight decrease until it, finally, reaches a saturation value at higher concentrations of bentazon.

The influence of the initial concentration of an organic compound on the photocatalytic degradation rate of most organic compounds is described by a pseudo-first order kinetics, which is rationalized in terms of the Langmuir-Hinshelwood model, modified to be valid for reactions occurring at a solid-liquid interface [37,38]:

$$r_0 = -\frac{dC}{dt} = \frac{k_r K C}{1 + KC} \quad (2)$$

where r_o is the initial degradation rate and C is the concentration of the organic substrate. K represents the equilibrium constant for adsorption of the organic substrate onto the semiconductor and k_r reflects the limiting rate constant of reaction at maximum coverage under the given experimental conditions. This equation can be used when data demonstrate linearity, plotted as follows:

$$\frac{C}{r_0} = \frac{1}{k_r K} + \frac{C}{k_r} \quad (3)$$

As indicated in the inset of Fig. 3, the plot of C/r_0, as a function of the initial concentration, C, yields for constant concentration of TiO_2 P25 at 0.5 g L^{-1} a straight line. The k_r and K values calculated according to Eq. (3) from the slope and the intercept with the C/r_o axis of the resulting straight line ($R^2 = 0.98$), were 0.48 ± 0.05 mg L^{-1} min^{-1} ($2 \times 10^{-6} \pm 0.21 \times 10^{-6}$ mol L^{-1} min^{-1}) and 0.62 ± 0.03 L mg^{-1} ($14.9 \times 10^4 \pm 0.72 \times 10^4$ L mol^{-1}), respectively.

3.4. Effect of solution's pH

Solution's pH, on the other hand, plays an important role in the photocatalytic degradation of various organic pollutants. Some properties of the photocatalyst, such as surface charge state and flat band potential are highly pH dependent, while electrostatic attraction or repulsion between the catalyst's surface and the organic molecule, depending on the ionic form of the organic compound (anionic or cationic) enhances or inhibits, respectively, the photodegradation rate [39–41]. Moreover, pH influences the size of TiO_2 aggregates, the interaction of the solvent molecules with the catalyst and the type of radicals or intermediates formed during the photocatalytic process. All of these factors influence the adsorption of organic molecules onto TiO_2 and affect the observed removal rates [42]. The effect of pH on bentazon's initial degradation rates has been studied and the results are displayed in Fig. 4. As pH increases from 3.0 to 6.0 (natural pH), the initial degradation rate, also increases by a factor of approximately 6, rendering 6.0 the most favorable pH value for the decomposition of the herbicide. However, degradation rates gradually decrease as photocatalysis

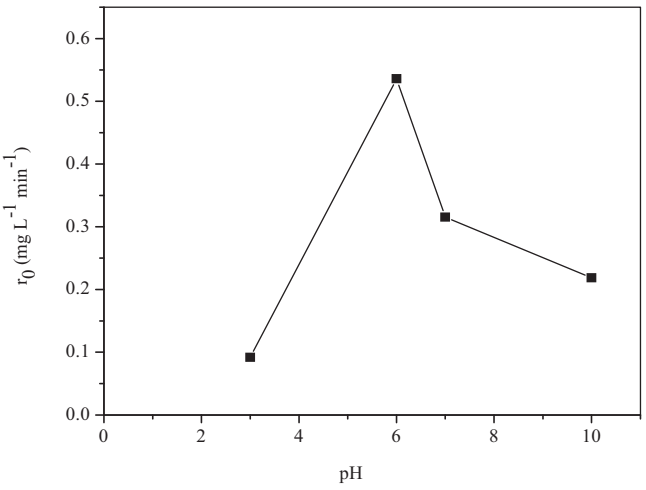

Fig. 4. Effect of pH in the initial degradation rate of 20 mg L^{-1} bentazon in the presence of 0.5 g L^{-1} TiO_2 P25 and UV-A.

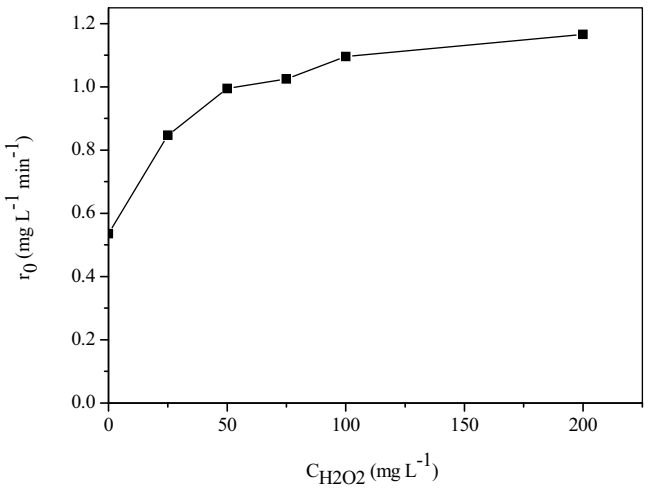

Fig. 5. Effect of H_2O_2 concentration in the initial degradation rate of 20 mg L^{-1} bentazon in the presence of 0.5 g L^{-1} TiO_2 P25 and UV-A.

takes place in progressively higher, neutral or alkaline pH values. Bentazon is a weak acid having a pKa value of 3.3 [6] thus, it exists predominantly in anionic form under natural aquatic environments [43]. Since TiO_2 has a zero point of charge (zpc) of approximately 6.35, the surface of TiO_2 is positively charged ($TiOH^+$) in solutions with a pH lower than 6.35, favorable for attracting anions and TiO_2 deprotonates in solutions with a pH higher than 6.35, hence its surface becomes negatively charged (TiO^-), favorable for repelling anions [44]. A further increase of pH, in particular beyond pzc_{TiO2} (6.35), results in accumulation of negative charges on the surface of TiO_2, causing repulsion of the negatively charged bentazon molecules. Thus, surface adsorption and initial degradation rates decrease (Fig. 4).

3.5. Effect of electron acceptors

The addition of species with the potential to capture the photogenerated electrons is an extensively studied procedure, often leading to acceleration of the photocatalytic degradation rate [17,45]. In this study, the effect of adding hydrogen peroxide or Fe^{3+} in the TiO_2 slurry during photocatalytic degradation of bentazon was evaluated.

Initially, photocatalytic oxidation of 20 mg L^{-1} bentazon in the presence of different H_2O_2 concentrations and 0.5 g L^{-1} TiO_2 P25 has been studied. The influence of H_2O_2 concentration on the initial rate of photo-oxidation of bentazon is shown in Fig. 5. Photocatalytic efficiency increases as the concentration of H_2O_2 increases and it reaches an optimum in the area of 100–200 mg L^{-1}.

In the absence of catalyst, the addition of 100 mg L^{-1} H_2O_2 into the irradiated aqueous solution gives a reaction rate value of 0.012 mg L^{-1} min^{-1} (Table 1), demonstrating that H_2O_2/UV-A failed to efficiently decompose bentazon. As demonstrated in Table 1, in the presence of 0.5 g L^{-1} TiO_2 P25, the introduction of H_2O_2 at a concentration of 100 mg L^{-1} seems to accelerate the process by a factor of ~2. This finding underlines the role of H_2O_2 as a promoter during photocatalytic degradation of bentazon employing TiO_2 P25. The observed enhancing effect can be owed to several reasons. H_2O_2 may accept a photogenerated electron from the conduction band, promoting charge separation (Eq. (4)). It may also form $OH^\bullet$ radicals via superoxide, according to Eq. (5):

$$H_2O_2 + e^- \rightarrow OH^- + OH^\bullet \quad (4)$$

$$H_2O_2 + O_2^{\bullet -} \rightarrow OH^\bullet + OH^- + O_2 \quad (5)$$

However, in the cases of ZnO, TiO_2 UV-100 and TiO_2 Kronos vlp 7000, the addition of H_2O_2 inhibits the photodegradation rate of bentazon (Table 1). A possible explanation for the difference between TiO_2 P25 and ZnO concerning the synergetic effect of H_2O_2 on the photocatalytic oxidation could be the extent of adsorption of H_2O_2 onto the semiconductor surface. Various studies show that in the case of ZnO the amount of H_2O_2 adsorbed onto the surface is negligible in comparison to the respective one in the case of TiO_2 [46,47]. As a consequence, the photogenerated electrons in TiO_2 suspensions can more easily reduce the adsorbed H_2O_2 molecules, leading to a lower e^-/h^+ recombination rate and thus, to a higher photocatalytic efficiency, in comparison to the respective processes in ZnO suspensions [48].

The initial degradation rate of TiO_2 UV-100 and TiO_2 Kronos vlp 7000 in the presence of 100 mg L^{-1} H_2O_2 was found to be 5.5 and 3 times lower, respectively, in comparison to the ones in the absence of the electron scavenger (Table 1). This discrepancy amongst TiO_2 P25 and the other two types of commercial catalysts could be attributed to differences in the BET surface, impurities, lattice mismatches or density of hydroxyl groups present on the catalyst's surface, that could affect the adsorption behaviour of degradation intermediates and the lifetime and recombination rate of electron–hole pairs. With these in mind, the dominant reactive species may vary depending on the type of TiO_2 particles employed thus, leading toward different reaction mechanisms [49]. The inhibiting effect of H_2O_2 may also be attributed to the scavenging effect of hydroxyl radicals by hydrogen peroxide and/or modification of the TiO_2 surface by H_2O_2 adsorption; H_2O_2 may compete with bentazon for the active sites onto TiO_2 particles, which ultimately leads to lower efficiency for bentazon photocatalytic degradation [50]. In addition, under air-equilibrated conditions, dissolved oxygen may also act as an electron scavenger, yielding superoxide radical anions which, in turn, react with protons (generated by valence-band holes reacting with water) to form peroxide radicals [51]. Similar behaviour has been previously reported for TiO_2 Kronos vlp 7000 in the case of methanol photodegradation [52].

Another factor that has been proven to enhance photocatalytic efficiency in various studies is the addition of metal ions in the semiconducting slurry [53]. In the present study, the effect of Fe^{3+} on the photocatalytic degradation of bentazon has been investigated. In the absence of catalyst, the addition of 7 mg L^{-1} Fe^{3+} into the irradiated aqueous solution results to a reaction rate value of 0.166 mg L^{-1} min^{-1} (Table 1). Bearing in mind that direct photol-

ysis of bentazon does not occur under the present experimental conditions, it can be concluded that the observed degradation in the absence of catalyst is owed exclusively to Fe^{3+} photodecomposition by irradiation and generation of hydroxyl radicals. The values of the initial reaction rates in Table 1 demonstrate that in the presence of 0.5 g L^{-1} TiO_2 P25, TiO_2 UV-100 and TiO_2 Kronos vlp 7000, the introduction of 7 mg L^{-1} Fe^{3+} accelerates the process. The observed enhancing effect could be attributed to interactions between iron species and TiO_2 [54]. There are three parallel processes of $OH^{\bullet}$ generation in the system which include iron species, which may be described by the following reactions. The first is a photocleavage of Fe^{3+} hydroxoaqua complex (Eq. (6)), the second is a reduction of photogenerated TiO_2 holes by ferrous ions returning the photoactive Fe^{3+} hydroxoaqua complexes and the third is a dark Fenton reaction (Eq. (7)) [55]:

$$Fe(OH)^{2+} + h\nu \rightarrow Fe^{2+} + OH^{\bullet} \quad (6)$$

$$Fe^{2+} + H_2O_2 + H^+ \rightarrow Fe^{3+} + OH^{\bullet} + H_2O \quad (7)$$

$$Fe^{3+} + TiO_2(e^-) \rightarrow Fe^{2+} + TiO_2 \quad (8)$$

The reaction of adsorbed Fe^{3+} with the photogenerated electrons (Eq. (8)) lowers the recombination rate of photogenerated holes and electrons resulting in an enhancement of the concentration of $OH^{\bullet}$ radicals [56]. Electron trapping by soluble Fe^{3+} aggregates has a positive effect because such species are easily reduced on the TiO_2 surface. Synergy is also affected by the concentration of TiO_2, of iron species, the system studied, etc. [57,58]. Meštankova et al. showed that it is possible to use more than a ten times lower concentration of TiO_2 photocatalyst in the presence of Fe^{3+} salt to reach the same photodegradation rate of monuron as for the corresponding TiO_2 system in the absence of Fe^{3+} [59]. It is well evidenced that in the Fe^{3+}/TiO_2/UV process, the adsorption of Fe^{3+} onto titania surface is the key reaction leading to synergy [60].

Overall, it can be concluded that the addition of H_2O_2 in the TiO_2 P25 slurry resulted in higher degradation rates in comparison to the ones where Fe^{3+} was employed as an electron acceptor. However, addition of H_2O_2 in the TiO_2 Kronos vlp 7000 or TiO_2 UV-100 suspension led to lower r_0 values, in comparison to the ones in the absence of peroxide, while the use of Fe^{3+} only marginally affected photocatalytic efficiency (Table 1).

3.6. Mineralization

Photocatalytic mineralization of bentazon proceeds through the formation of various reaction intermediates, whose carbon atoms are eventually converted to carbon dioxide, while heteroatoms are converted to inorganic ions that remain in the liquid phase. Bentazon mineralization can be described by the following overall reaction scheme:

$$C_{10}H_{12}N_2O_3S + 17O_2 \rightarrow 10CO_2 + 2HNO_3 + 2H_2SO_4 + 3H_2O \quad (9)$$

Fig. 6 shows the extent of the dissolved organic content (DOC) reduction vs. illumination time of a solution containing 20 mg L^{-1} bentazon in the presence of 0.5 g L^{-1} TiO_2 P25 or Kronos vlp 7000, alone or with the addition of 100 mg L^{-1} H_2O_2. In the presence of TiO_2 P25, 85% of the initial carbon content in bentazon was converted to CO_2 during the first 120 min. The addition of 100 mg l^{-1} H_2O_2 in the TiO_2 P25 suspension accelerates the photomineralization process of bentazon, especially at the beginning of the reaction, a finding that is in agreement with the respective photodegradation experiments (Table 1).

In the case of C-doped TiO_2 Kronos vlp 7000, DOC increases during the first 60 min of the photomineralization process, possibly due to carbon leaching phenomena. Then, mineralization proceeds, however, with lower efficiency compared to the one in the presence

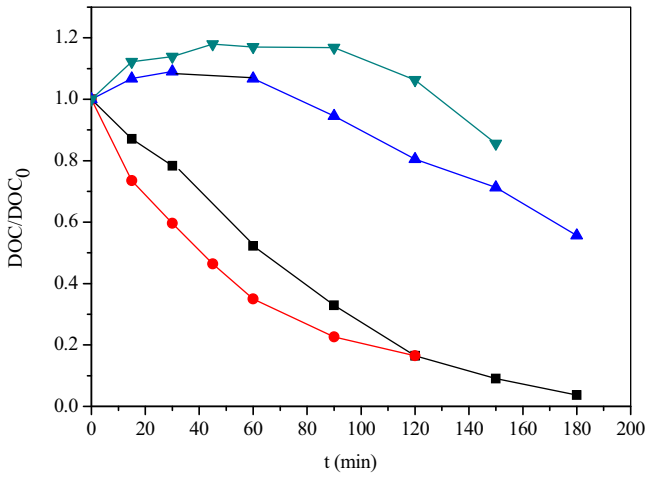

Fig. 6. Photocatalytic mineralization of 20 mg L^{-1} of bentazon in the presence of UV-A and: (■) 0.5 g L^{-1} TiO_2 P25, (●) 0.5 g L^{-1} TiO_2 P25 and 100 mg L^{-1} H_2O_2, (▲) 0.5 g L^{-1} TiO_2 Kronos vlp 7000, (▼) 0.5 g L^{-1} TiO_2 Kronos vlp 7000 and 100 mg L^{-1} H_2O_2.

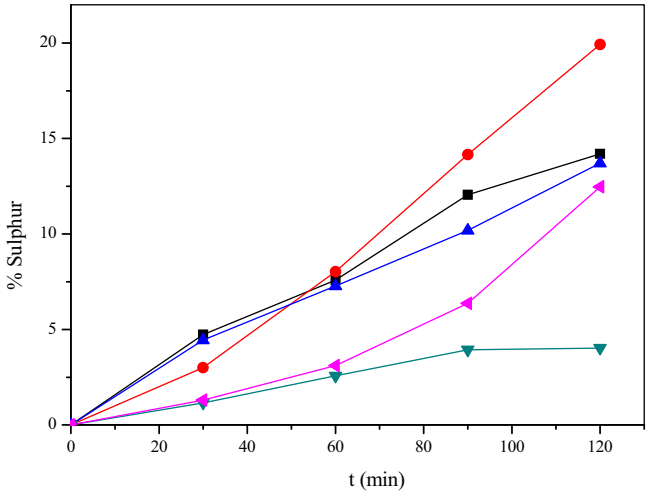

Fig. 7. Release of sulfur during photocatalytic mineralization of 20 mg L^{-1} bentazon in the presence of UV-A: (■) 0.5 g L^{-1} TiO_2 P25, (●) 0.5 g L^{-1} TiO_2 P25, 100 mg L^{-1} H_2O_2, (▲) 0.5 mg L^{-1} TiO_2 Kronos vlp 7000, (▼) 0.5 g L^{-1} TiO_2 Kronos vlp 7000, 100 mg L^{-1} H_2O_2, (◄) 0.5 g L^{-1} TiO_2 Kronos vlp 7000 and visible light.

of TiO_2 P25 and after 180 min of illumination only 45% of the initial DOC in the bentazon molecule has been converted to CO_2. Mineralization rates are further reduced when H_2O_2 is added in the TiO_2 Kronos vlp 7000 slurry, similarly to the respective photodegradation experiments (Table 1).

Figs. 7 and 8 show temporal profiles of sulfur and total inorganic nitrogen (i.e. contained in nitrates, nitrites and ammonium ions), respectively, released during photocatalytic oxidation of bentazon. Profiles do not show actual concentrations but they correspond to the percentage of the theoretical amount of sulfur or nitrogen initially present in the molecule.

Organic sulfur is only partly converted into inorganic in the presence of TiO_2 P25 (almost 14.2% conversion within 120 min of illumination, Fig. 7). TiO_2 Kronos vlp 7000, under the same experimental conditions, leads to only slightly lower conversion rate, both when UV-A or visible are employed as illumination sources (13.7 and 12.5% respectively). Sulfur conversion is enhanced when H_2O_2 is added in the reaction mixture in the presence of TiO_2 P25, reaching almost 20%. However, addition of H_2O_2 inhibits the efficiency of TiO_2 vlp K7000, resulting to lower conversion rates.

Fig. 8 shows concentration–time profiles of total inorganic nitrogen (i.e. the sum of nitrogen contained in NO_3^-, NH_4^+ and NO_2^-)

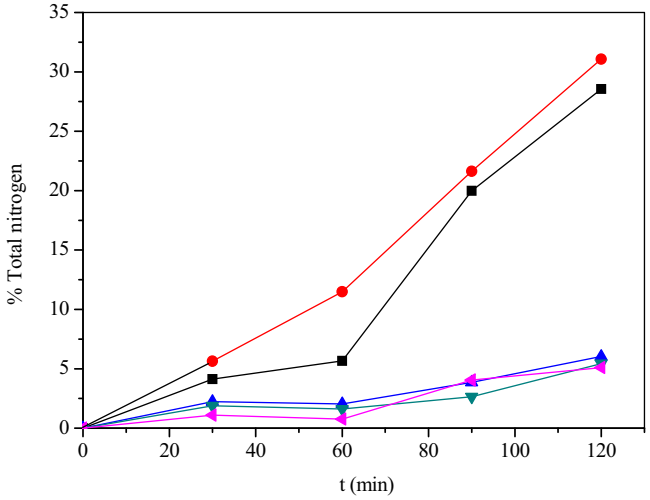

Fig. 8. Release of total nitrogen during photocatalytic mineralization of 20 mg L^{-1} bentazon in the presence of UV-A: (■) 0.5 g L^{-1} TiO_2 P25, (●) 0.5 g L^{-1} TiO_2 P25, 100 mg L^{-1} H_2O_2, (▲) 0.5 mg L^{-1} TiO_2 Kronos vlp 7000, (▼) 0.5 g L^{-1} TiO_2 Kronos vlp 7000, 100 mg L^{-1} H_2O_2, (◄) 0.5 g L^{-1} TiO_2 Kronos vlp 7000 and visible light.

as percentage of the theoretical nitrogen in bentazon, under various experimental conditions. In all cases, ammonium and nitrate were the dominant inorganic species formed during photocatalytic degradation, while trace amounts of NO_2^- were detected which, upon prolonged irradiation, were oxidized to NO_3^-. Organic nitrogen is only partly converted into inorganic in the presence of TiO_2 P25 under the conditions employed in the study (28.5% conversion within 120 min of illumination, Fig. 8). The addition of 100 mg L^{-1} H_2O_2 slightly enhances the process, leading to 31% conversion. On the other hand, TiO_2 Kronos vlp 7000 alone or in the presence of H_2O_2, failed to effectively convert organic nitrogen into inorganic species, resulting to approximately 6% conversion within 120 min of UV-A illumination. Similar results were obtained in the presence of TiO_2 Kronos vlp 7000 and visible light.

3.7. Transformation products and reaction pathways

3.7.1. Identification of transformation products

Identification of TPs during heterogeneous photocatalytic oxidation of bentazon was investigated, aiming also to the elucidation of the potential degradation mechanisms that occur during this process. Samples were collected after photocatalytic oxidation of the herbicide in the presence of 0.5 g L^{-1} TiO_2/UV-A, without the addition of H_2O_2, aiming to the detection of a high number of TPs. A first screening for candidate TPs was performed in a LC-DAD-ESI/MS system. Numerous TPs were detected showing several structurally diagnostic ions (Supporting information, Fig. SI-1). However, to better understand chemical diversity of the formed TPs and to distinguish the high number of isobaric species, a high resolution MS instrument was further used. Acquisition in full scan mode was performed in the range m/z 50–700. Such a wide range of m/z was scanned in order to look for dimers, since dimerization has been previously reported to occur during phototransformation of organic contaminants [61,62]. The high resolving power endorsed by a linear ion trap (LIT) Orbitrap LC-ESI/MS system allowed detection of up to 21 TPs generated during TiO_2/UV-A photocatalytic oxidation of bentazon.

Most TPs were eluted earlier than the parent molecule, underlying the formation of more polar compounds, contrary to the detected dimmer derivatives. Their elemental compositions and chemical structures were tentatively proposed based on the accurate mass information obtained by high resolution LC–MS, MS^2 and MS^3 fragmentation, and on mass spectral comparisons with the parent compound. Experimental and theoretical masses (m/z), the error between them in mDa and mg L^{-1}, retention times (t_R), the double bond equivalent (DBE), the proposed elemental composition of the TPs and their main fragment ions are shown in Table 2.

The product ions arising from the pseudo-molecular ion of bentazon (m/z 239.0495, $C_{10}H_{11}O_3N_2S^-$) are demonstrated in Table 2 and Fig. SI-2. MS^2 spectra showed as key fragmentation pathways, the loss of the isopropyl group and of sulfur dioxide with subsequent ring closure and the formation of the product ions at m/z 197.0026 ($C_7H_5O_3N_2S^-$) and 175.0876 ($C_{10}H_{11}ON_2^-$), respectively. The loss of both groups produces the fragment with m/z 132.0329 ($C_7H_4N_2O^-$), while the product ion at m/z 147.0815 ($C_{10}H_{11}O^-$) originates from the product at m/z 175.0876 by the loss of N_2 (28.0061 Da). These pathways have been carefully considered in the structure attribution of unknown species presented below.

The identified TPs (Figs. SI-1, SI-3 and SI-4), can be classified into four principal groups according to their proposed structures and transformation pathways: i) hydroxy and/or keto bentazon derivatives (Fig. 9, routes a and b), ii) SO_3-bentazon derivatives (Fig. 9, route c), iii) TPs arising from the detachment of the isopropyl group (Fig. 9, route d) and iv) dimer bentazon derivatives (Fig. 9, route e). The assignment of the TPs' structure is discussed in detail in the next section based on the accurate mass values (m/z).

3.7.1.1. Hydroxy and/or keto bentazon derivatives. These species are the main intermediates during the first stages of photocatalytic degradation as a consequence of the $OH^\bullet/O_2^{\bullet-}$ radical attack on the bentazon molecule. Starting with the ion with m/z 255.0445, three isomers with retention times (t_R) between 1.60 and 1.74 min and a pseudo-molecular formula of $C_{10}H_{11}O_4N_2S$-(|D (error)| <5 mg L^{-1}) have been detected. These findings are consistent with the addition of a hydroxyl group in different positions in the parent compound, to yield monohydroxylated derivatives [63–66]. The fragmentation pattern of these three compounds enabled detection of the different positions of the hydroxyl group. For example, MS^2 fragmentation of the monohydroxylated isomer ($C_{10}H_{11}O_4N_2S^-$) at t_R 1.60 min (iPr-OH-BNZ, Table 2), exhibited key fragments at m/z 197.0026, 191.0829, 175.0876 and 132.0329. The fragment with m/z 197.0026 ($C_7H_5O_3N_2S^-$) results from the loss of the hydroxylated isopropyl group, while the fragment with m/z 191.0829 ($C_{10}H_{11}O_2N_2^-$) derives from the loss of SO_2 and the subsequent ring closure. Similarly to bentazon fragmentation, the loss of both groups produces the fragment with m/z 132.0329 ($C_7H_4N_2O^-$), suggesting that this product (iPr-OH-BNZ) could be attributed to hydroxylated bentazon on one of the two methyl groups of the isopropyl moiety. The other two isomers (Ring-OH-BNZ_A and Ring-OH-BNZ_B) exhibit key fragment ions at m/z 191.0829 ($C_{10}H_{11}O_2N_2^-$), 148.0278 ($C_7H_4N_2O_2^-$) and 132.0329 ($C_7H_4N_2O^-$), which well match with a modified aromatic ring. For example, the fragment at m/z 148.0278 derives from the loss of the isopropyl and SO_2 groups, suggesting that these products reasonably hold the OH group in the aromatic ring. Similar observations regarding the $OH^\bullet$ attack on the isopropyl moiety or on the aromatic ring have already been described regarding the photolytic and photocatalytic treatment of bentazon [63–66].

Continuous $OH^\bullet$ attack leads to the formation of more hydroxylated TPs. The peaks corresponding to double hydroxylation appear at three distinct retention times, confirming that the reaction can occur at several different sites (aromatic ring or methyl groups attached to the isopropyl moiety). These isomers yield a theoretical accurate mass m/z of 271.0394 (TP-271_A, 271_B, 271_C), leading to the best-fit pseudo molecular formula of $C_{10}H_{11}O_5N_2S^-$. Despite the observed differences in the MS^2 fragmentation pattern, all species showed the key loss of SO_2, generating the product ion at m/z

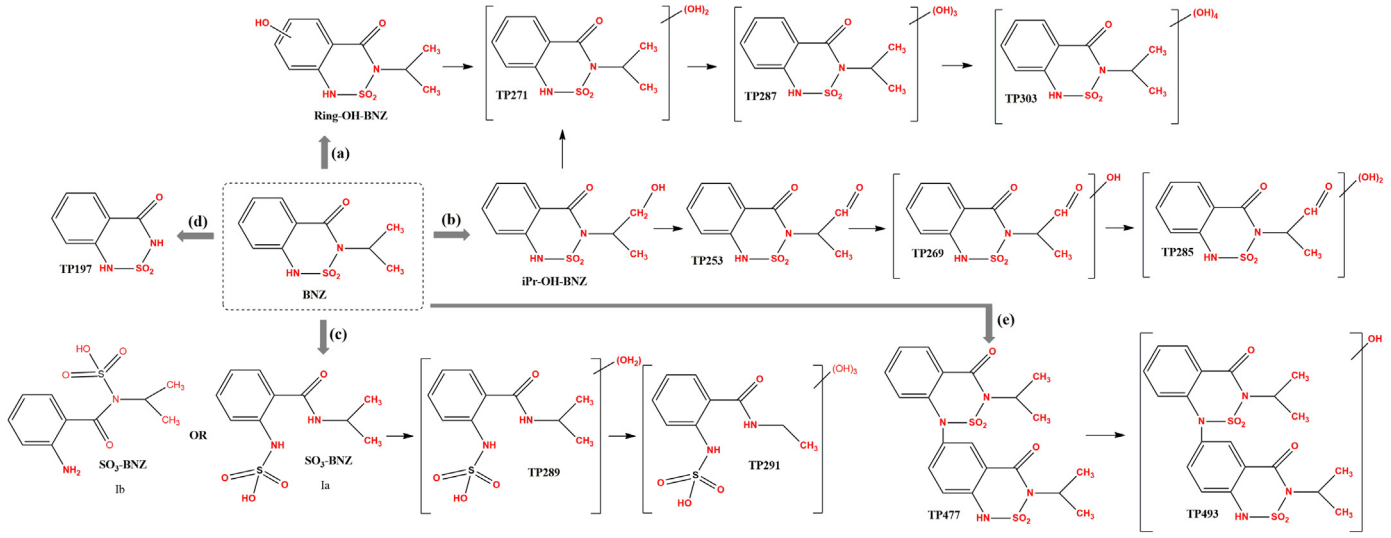

Fig. 9. Proposed transformation pathways during TiO_2 mediated photocatalytic oxidation of bentazon (0.5 g L^{-1} TiO_2 P25, UV-A).

207.0775 ($C_{10}H_{11}O_3N_2^-$). For TP-271$_A$ and TP-271$_B$, the product ion at *m/z* 243.0445 consistent with the formula $C_9H_{11}O_4N_2S^-$ was also observed, implying the loss of CO (27.9949 Da) from the product molecule. Hydroxylation can proceed even further resulting to the formation of tri-hydroxyl isomers (TP-287 with *m/z* 287.0343) and tetra-hydroxy (TPs-303$_A$ and 303$_B$ with *m/z* 303.0292) isomers. Further oxidation on aromatic ring or on methyl groups attached to the isopropyl moiety results to the hydroxyl/keto-derivatives with accurate mass at *m/z* 253.0289 (TP-253), 269.0232 (TP-269) and 285.0195 (TP-285).

It should be pointed out that for many of the above species the mass spectra data was not enough to attribute the exact position for hydroxylation and/or demethylation. Some tentative structures have been proposed in pathways of Fig. 9.

3.7.1.2. SO_3-bentazon derivatives. An additional transformation pathway involved the formation of the *m/z* ion 257.0601, with empirical formula $C_{10}H_{13}O_4N_2S^-$, well matched with the sulfamic acid derivative (SO_3-BNZ). MS^2 spectrum, exhibited the key MS^2 product ion at *m/z* 177.1033 ($C_{10}H_{13}ON_2^-$) which can be easily assigned to SO_3 group elimination (79.9568 Da). The fragmentation spectra obtained do not allow identification of the exact position (N- or N′-position) concerning the sulfur–nitrogen bond cleavage. However, based on steric effects, a cleavage at the N position (Fig. 9, compound Ia) seems more likely than at the N′-position (Fig. 9, compound Ib). The same TP was also suggested in other photodegradation studies of bentazon [64,65].

3.7.1.3. TPs arising from the detachment of the isopropyl group. An additional transformation pathway involved the formation of the *m/z* ion 197.0026 (TP-197), with empirical formula $C_7H_5O_3N_2S^-$ well matched with the detachment of the isopropyl moiety. MS^2 spectrum, exhibited a key ion at *m/z* 133.0407 ($C_7H_5ON_2^-$) suggesting the typical loss of sulfur dioxide and the subsequent ring closure. Further transformation could lead to the formation of products by cleavage of the rings. For instance, the TP at *m/z* 191.0132 (TP-191, $C_5H_7O_4N_2S^-$) would probably be formed via the rupture of the aromatic ring. The main ion observed during its fragmentation (*m/z* 163.0183) corresponds to the loss of CO (observed 27.9947; calculated 27.9949). However, the structural elucidation of TP-191 was not possible.

3.7.1.4. Dimers and hydroxylated derivatives. Combinations of dimerization and hydroxylation reactions represent another major transformation pathway during TiO_2 mediated photocatalytic oxidation of bentazon. Dimerization of bentazon and its phototransformation products has been previously observed during phototransformation experiments in soils [67] and plant leaves after crop treatment [64]. Interestingly, dimerization of bentazon has not been reported in previous photocatalytic studies in aqueous media. Here, a dimer-bentazon derivative showed a pseudo-molecular ion at *m/z* 477.0908 (TP-477), fitted to $C_{20}H_{21}O_6N_4S_2^-$. The main ions observed during its fragmentation (*m/z* 435.0438 and 413.1289) correspond to the loss of the isopropyl group and of sulfur dioxide with subsequent ring closure resulting to the formation of the product ions at *m/z* 413.1289 thus, following the same fragmentation pattern as bentazon. Further oxidation leads to the formation of two isobaric dimer bentazon products with an accurate mass of 493.0852 (TP-493$_A$ and 493$_B$, $C_{20}H_{21}O_7N_4S_2^-$). These species show a different fragmentation pattern indicating the non-selective attack of OH•. The fragmentation of TP-493A is characterized by the presence of two main fragment ions with calculated exact masses of *m/z* 451.0387 and 429.1238, corresponding to formulas $C_{17}H_{15}O_7N_4S_2^-$ and $C_{20}H_{21}O_5N_4S^-$, respectively. The ion at *m/z* 451.0387 results from the loss of the isopropyl group, whereas the ion at *m/z* 429.1238 corresponds to the typical loss of SO_2 (63.9619 Da). Finally, *m/z* 387.0768 derives from the sequential detachment of the second isopropyl chain from the ion at *m/z* 429.1238. The second isobaric dimer compound (TP-493$_B$) exhibits the same fragment ion (*m/z* 429.1238) as TP-493$_A$, which corresponds to the characteristic loss of SO_2 group. Subsequent loss of the second SO_2 group will result to the fragment ion at *m/z* 365.1619 with best fit formula of $C_{20}H_{21}O_3N_4^-$. Unfortunately, there is not enough information to properly locate the oxidized moiety for these isobaric species.

3.7.2. Evolution of TPs' profiles and proposed transformation pathways

In order to acquire more information on the main photocatalytic transformation routes, the evolution profiles of the TPs formed during TiO_2/UV-A mediated photocatalytic oxidation of bentazon were obtained. Since chemical standards were not available for their quantitative analysis, evolution of TPs is depicted as a function of the peak area obtained in the LC analysis vs. irradiation time.

Table 2
MS^2 (black color) and MS^3 (blue color) data and detected transformation products (TPs), formed during TiO_2 mediated photocatalytic oxidation (0.5 g L^{-1} TiO_2 P25, UV-A) of bentazon (BNZ).

Compound	t_R (min)	Elemental composition	Exact mass (*m/z*, theoretical)	Accurate/ nominal mass (*m/z*, detected)	Error (mDa)	Error (mg L^{-1})	DBE
BNZ	**1.81**	**C_{10} H_{11} O_3 N_2 S**	**239.0495**	**239.0497**	**0.11**	**0.46**	**6.5**
		C_7 H_5 O_3 N_2 S	197.0026	197.0029	0.26	1.33	6.5
		C_{10} H_{11} O N_2	175.0876	175.0881	0.41	2.3	6.5
		C_{10} H_{11} O	147.0815	147.0822	0.66	4.96	5.5
		C_7 H_4 N_2 O	132.0329	132.0336	0.68	5.21	7.0
	MS^3	C_7 H_5 O_3 N_2 S	197.0026	197.0029	0.26	1.33	6.5
		C_7 H_5 O N_2	133.0407	133.0416	0.86	6.49	6.5
	MS^3	C_{10} H_{11} O N_2	175.0876	175.0881	0.41	2.3	6.5
		C_{10} H_{11} O	147.0815	147.0818	0.26	1.77	5.5
		C_7 H_4 N_2 O	132.0329	132.0333	0.38	2.94	7.0
TP-303$_A$	**1.30**	**C_{10} H_{15} O_7 N_2 S**	**303.0292**	**303.0295**	**0.25**	**0.83**	**6.5**
		C_9 H_{11} O_5 N_2 S	259.0394	259.0391	-0.31	-1.22	5.5
		C_8 H_{11} O_3 N_2 S	215.0495	215.0496	0.01	0.05	4.5
TP-303$_B$	**1.33**	**C_{10} H_{15} O_7 N_2 S**	**303.0292**	**303.0295**	**0.25**	**0.83**	**6.5**
		C_{10} H_{11} O_5 N_2 S	271.0394	271.0393	-0.12	-0.43	6.5
TP-291	**1.36**	**C_9 H_{11} O_7 N_2 S**	**291.0292**	**291.0295**	**0.25**	**0.87**	**5.5**
		C_8 H_{11} O_5 N_2 S	247.0394	247.0393	-0.11	-0.47	4.5
		C_7 H_9 O_5 N_2 S	233.0237	233.0238	0.03	0.14	4.5
		C_8 H_{11} O_3 N_2	183.0775	183.0777	0.18	1.00	4.5
		C_7 H_{11} O_2 N_2	155.0826	155.0824	-0.20	-1.30	3.5
TP-289$_A$	**1.45**	**C_{10} H_{13} O_6 N_2 S**	**289.0499**	**289.0501**	**0.11**	**0.41**	**5.5**
		C_{10} H_{11} O_5 N_2 S	271.0394	271.0393	-0.12	-0.43	6.5
		C_9 H_{11} O_4 N_2 S	243.0445	243.0446	0.09	0.40	5.5
TP-289$_B$	**1.53**	**C_{10} H_{13} O_6 N_2 S**	**289.0499**	**289.0501**	**0.11**	**0.41**	**5.5**
		C_{10} H_{10} O_4 N_2 S	254.0366	254.0369	0.22	0.87	7.0
		C_7 H_5 O_3 N_2 S	197.0026	197.0029	0.26	1.33	6.5
TP-287	**1.59**	**C_{10} H_{11} O_6 N_2 S**	**287.0343**	**287.0343**	**-0.03**	**-0.11**	**6.5**
		C_9 H_{11} O_5 N_2 S	259.0392	259.0392	-0.21	-0.83	5.5
		C_{10} H_{11} O_4 N_2	223.0724	223.0734	0.96	4.34	6.5
		C_9 H_{11} O_3 N_2	195.0775	195.0777	0.18	0.94	5.5
		C_9 H_9 O_2 N_2	177.0669	177.0668	-0.15	-0.85	6.5

Table 2 *Continued*

		$C_8 H_{10} O_2 N$	152.0717	152.0727	0.99	6.56	4.5
TP-285	**1.38**	**$C_{10} H_9 O_6 N_2 S$**	**285.0186**	**285.0195**	**0.41**	**1.46**	**7.5**
		$C_9 H_9 O_5 N_2 S$	257.0237	257.0235	-0.26	-1.03	6.5
		$C_{10} H_9 O_4 N_2$	225.0567	225.565	-0.28	-1.26	7.5
TP-271$_A$	**1.50**	**$C_{10} H_{11} O_5 N_2 S$**	**271.0394**	**271.0394**	**-0.02**	**-0.06**	**6.5**
		$C_9 H_{11} O_4 N_2 S$	243.0445	243.0444	-0.10	-0.42	5.5
		$C_{10} H_{11} O_3 N_2$	207.0775	207.0776	0.06	0.41	6.5
		$C_7 H_4 O_3 N$	150.0196	150.0204	0.73	4.88	6.5
		$C_6 H_4 O_2 N$	122.0247	122.0253	0.54	4.49	5.5
TP-271$_B$	**1.63**	**$C_{10} H_{11} O_5 N_2 S$**	**271.0394**	**271.0394**	**-0.02**	**-0.06**	**6.5**
		$C_{10} H_9 O_4 N_2 S$	253.0288	253.0289	0.05	0.19	7.5
		$C_9 H_{11} O_4 N_2 S$	243.0445	243.0444	-0.10	-0.42	5.5
		$C_{10} H_{11} O_3 N_2$	207.0775	207.0776	0.06	0.41	6.5
TP-271$_C$	**1.70**	**$C_{10} H_{11} O_5 N_2 S$**	**271.0394**	**271.0394**	**-0.02**	**-0.06**	**6.5**
		$C_{10} H_{11} O_3 N_2$	207.0775	207.0776	0.06	0.41	6.5
TP-269	**1.72**	**$C_{10} H_{11} O_5 N_2 S$**	**269.0237**	**269.0232**	**-0.56**	**-2.1**	**7.5**
		$C_9 H_9 O_4 N_2 S$	241.0288	241.0287	-0.15	-0.63	6.5
SO_3-BNZ	**1.56**	**$C_{10} H_{13} O_4 N_2 S$**	**257.0601**	**257.0584**	**-1.75**	**-6.81**	**5.5**
		$C_{10} H_{13} O N_2$	177.1033	177.1037	0.36	2.05	5.5
iPr-OH-BNZ	**1.60**	**$C_{10} H_{11} O_4 N_2 S$**	**255.0445**	**255.0449**	**0.39**	**1.565**	**6.5**
		$C_7 H_5 O_3 N_2 S$	197.0026	197.0029	0.26	1.33	6.5
		$C_{10} H_{11} O_2 N_2$	191.0829	191.0826	0.30	1.56	6.5
		$C_{10} H_{11} O N_2$	175.0876	175.0881	0.41	2.3	6.5
		$C_7 H_4 N_2 O$	132.0329	132.0333	0.38	2.94	7.0
Ring-OH-BNZ$_A$	**1.67**	**$C_{10} H_{11} O_4 N_2 S$**	**255.0445**	**255.0449**	**0.39**	**1.565**	**6.5**
		$C_{10} H_{11} O_2 N_2$	191.0829	191.0826	0.30	1.56	6.5
		$C_7 H_4 N_2 O_2$	148.0278	148.0286	0.77	5.22	7.0
		$C_7 H_4 N_2 O$	132.0329	132.0333	0.38	2.94	7.0
Ring-OH-BNZ$_B$	**1.74**	**$C_{10} H_{11} O_4 N_2 S$**	**255.0445**	**255.0449**	**0.39**	**1.565**	**6.5**
		$C_{10} H_{11} O_2 N_2$	191.0829	191.0826	0.30	1.56	6.5
		$C_7 H_4 N_2 O_2$	148.0278	148.0286	0.77	5.22	7.0
		$C_7 H_4 N_2 O$	132.0329	132.0333	0.38	2.94	7.0
TP-253	**1.57**	**$C_{10} H_9 O_4 N_2 S$**	**253.0288**	**253.0289**	**0.05**	**0.19**	**7.5**
		$C_{10} H_9 O_2 N_2$	189.0699	189.0671	0.14	0.79	7.5

Table 2 *Continued*

		$C_9 H_9 O_3 N_2 S$	225.0339	225.0338	-0.13	-0.61	6.5
TP-197	**1.25**	**$C_7 H_5 O_3 N_2 S$**	**197.0026**	**197.0031**	**0.46**	**2.35**	**6.5**
		$C_7 H_5 O N_2$	133.0407	133.0416	0.86	6.49	6.5
TP-191	**1.65**	**$C_5 H_7 O_4 N_2 S$**	**191.0132**	**191.0132**	**-0.00**	**-0.01**	**3.5**
		$C_4 H_7 O_3 N_2 S$	163.0183	163.0185	0.21	1.31	2.5
Dimers							
TP-477	**7.24**	**$C_{20} H_{21} O_6 N_4 S_2$**	**477.0908**	**477.0908**	**-0.0**	**-0.00**	**12.5**
		$C_{17} H_{15} O_6 N_4 S_2$	435.0438	435.0432	-0.65	-1.49	12.5
		$C_{20} H_{21} O_4 N_4 S$	413.1289	413.1280	-0.90	-2.1	12.5
TP-493$_A$	**5.27**	**$C_{20} H_{21} O_7 N_4 S_2$**	**493.0857**	**493.0852**	**-0.16**	**-0.03**	**12.5**
		$C_{17} H_{15} O_7 N_4 S_2$	451.0387	451.0374	-1.36	-3.09	12.5
		$C_{20} H_{21} O_5 N_4 S$	429.1238	429.1232	-0.61	-1.43	12.5
		$C_{17} H_{15} O_5 N_4 S$	387.0768	387.0760	-0.86	-2.23	12.5
TP-493$_B$	**7.01**	**$C_{20} H_{21} O_7 N_4 S_2$**	**493.0857**	**493.0852**	**-0.16**	**-0.03**	**12.5**
		$C_{20} H_{21} O_5 N_4 S$	429.1238	429.1231	-0.71	-1.66	12.5
		$C_{20} H_{21} O_3 N_4$	365.1619	365.1620	-0.01	-0.04	12.5

Typical bell-shaped profiles were obtained in most cases (Fig. 10). All TPs identified, reached maximum intensity within 60 min of illumination with different evolution rates. Afterwards, the amounts of all TPs were decreased and were subsequently completely degraded at the end of the photocatalytic process.

Fig. 9 shows the main proposed transformation pathways of bentazon during the TiO_2/UV-A photocatalytic process. Taking into account the identified TPs and their abundance, the primary phototransformation pathway proceeds via multistep hydroxylation reactions (routes a & b) via $OH^\bullet$ attack, producing monohydroxylated derivatives of bentazon (TP-255$_A$, 255$_B$, 255$_C$) and multihydroxylated (TP-271, TP-287, TP-303) and/or keto derivatives (TP-253, TP-269, TP-285). Routes c and d, leading to the formation of SO_3-bentazon and TP-197, were other parallel transformation pathways during heterogeneous photocatalysis. Dimerization and further hydroxylation of bentazon (route e) also took place during the phototransformation treatment (TP-277, TP-493$_A$, 493$_B$). After prolonged irradiation, the obtained TPs are further decomposed into other low-molecular weight products (aliphatic products, e.g., carboxylic acids etc.) by cleavage of their aromatic ring.

The reaction pathways proposed here, although with some similarities in some cases, differ from others previously reported in the literature. For example, in the study by Davezza et al. [63], transformation occurs mainly due to the $OH^\bullet$ attack on the aromatic ring or the methyl groups of the isopropyl moiety by the formation of hydroxy derivatives (e.g. TP-255, TP-253). However, formation of di and trihydroxylated or keto derivatives as well as of SO_3-bentazon and dimer derivatives was not observed. Finally, in the TiO_2 photocatalytic treatment of bentazon reported by Mir et al. [20], the herbicide showed different reaction pathways, leading mainly to desulfonated and nitro derivatives as well as to other breakdown products. However, these products were not detected in the present study. The obvious differences obtained between our proposed transformation pathways and those previously published may be attributed, among others, to the different analytical instrumentation used. For instance, in the study of Davezza et al. [63] an HPLC/MS system was used, while Mir et al. employed a GC–MS system. In our study, the high resolving power endorsed by the LIT-Orbitrap LC-ESI/MS system enabled the discrimination between isobaric species and ions of interest, providing accurate mass determination, both for the precursor *m*/*z* ions of the target TPs and for their fragmentation products.

3.8. Toxicity evaluation

The evaluation of potential toxicity of the samples before and during heterogeneous photocatalytic oxidation of bentazon was conducted by means of i) acute toxicity determination using *V. fisheri* marine bacteria and ii) phytotoxicity employing higher plant species (*Sinapis alba*, *Lepidium sativum*, *Sorghum saccharatum*). This investigation is of special interest since, several studies have clearly demonstrated that the photocatalytically generated intermediates may exhibit a more toxic effect than the parent compound [68].

3.8.1. Acute toxicity evaluation by V. fisheri

Aquatic toxicity is an important parameter in assessing the potential adverse effects of chemicals on aquatic species and ecosystems. Thus, the acute toxicity of bentazon and its transformation products was evaluated by monitoring changes in the natural emission of the luminescent marine bacteria *V. fischeri*, when challenged with aqueous solutions of bentazon, prior to and during

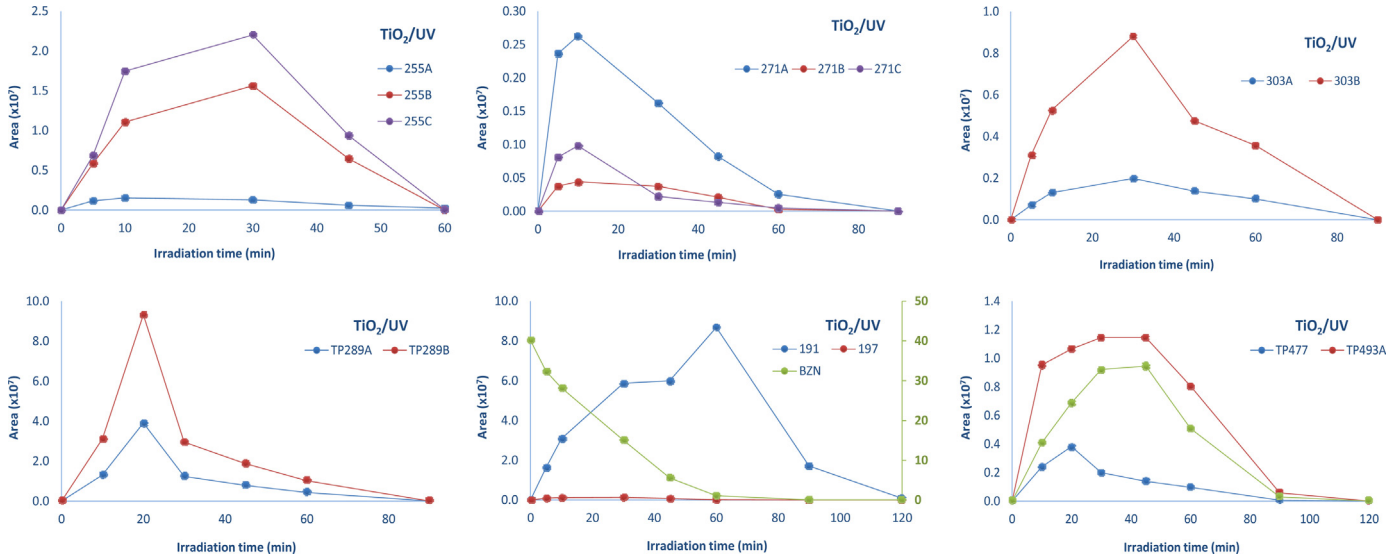

Fig. 10. Time evolution profiles of major transformation products (TPs) formed during TiO_2 mediated photocatalytic oxidation of bentazon (0.5 g L^{-1} TiO_2 P25, UV-A).

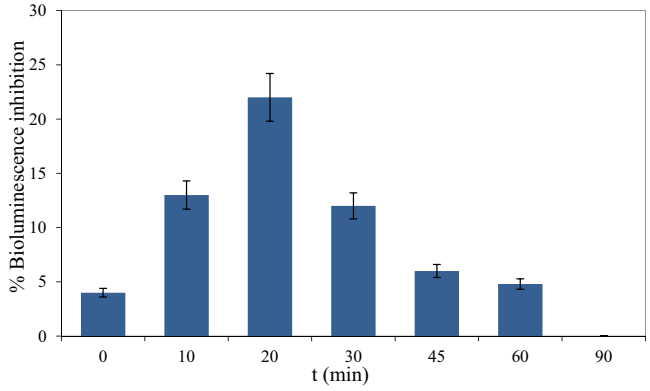

Fig. 11. Ecotoxicity profile of bentazon and its transformation products (TPs) based on *V. fisheri* bioluminescence measurements, during photocatalytic oxidation of bentazon (0.5 g L^{-1} TiO_2 P25, UV-A).

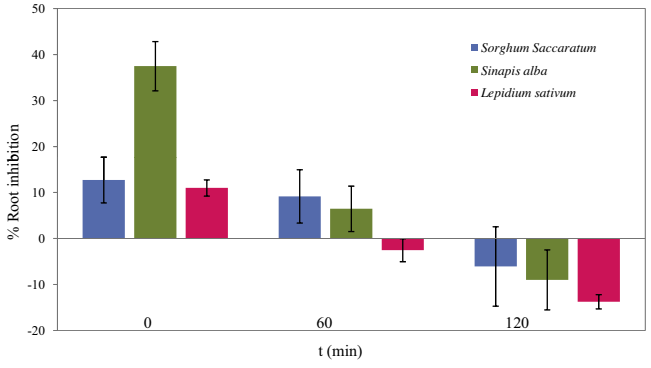

Fig. 12. Effect of 20 mg L^{-1} bentazon to the length of the root system of the plants: *S. saccharatum*, *S. alba* and *L. sativum* during photocatalytic treatment of the herbicide in the presence of 0.5 g L^{-1} TiO_2 P25 and UV-A irradiation.

TiO_2/UV-A mediated photocatalytic oxidation and it was expressed as percentage of inhibition of the bacteria luminescence (Fig. 11).

Bentazon solution with initial concentration of 20 mg L^{-1} showed a low inhibition value of 4%. Upon UV-A irradiation in the presence of 0.5 g L^{-1} TiO_2 P25, toxicity progressively increased, reaching a maximum of 22% inhibition at 20 min. Afterwards, toxicity is smoothly decreased, reaching approximately 5% at 60 min of irradiation. It must be pointed out that the highest toxicity is observed at irradiation times where all the identified TPs are present and the majority of them reach their maximum concentration (Fig. 10). Based on these findings we can assume that the higher toxicity at the first stages of treatment could be attributed to the formation of more toxic intermediates as well as on synergistic effects between them. However, at 90 min of illumination complete detoxification of the irradiated solution is achieved, demonstrating the efficiency of the proposed photocatalytic treatment in the elimination of acute ecotoxicity of bentazon under the investigated conditions.

3.8.2. Phytotoxicity evaluation by eukaryotic plant species

Phytotoxicity evaluation was conducted on samples taken during the photocatalytic process (0.5 g L^{-1} TiO_2 P25, UV-A) at various time points (0–120 min). Growth inhibition was not observed in any of the three types of seeds, therefore the study was focused on the calculation of root inhibition (RI). The treated samples displayed a variation of toxicity profiles on each type of plant examined, as shown in Fig. 12.

Root inhibition (RI) profile of bentazon during photocatalysis in the presence of 0.5 g L^{-1} TiO_2 P25 and UV-A irradiation, is different for the three species. The RI of the initial bentazon solution was relatively low for *S. saccharatum* (12.72 ± 4.98%) and *L. sativum* (11 ± 1.76%), while for *S. alba* it was significantly higher (37.48 ± 5.37%). For *S. saccharatum* at 60 min of treatment, the RI value demonstrated a small decrease in comparison to the initial bentazon solution. After 120 min of photocatalytic treatment an eutrophication of the roots of the plant takes place as demonstrated by the negative value of RI (−6.07 ± 8.64%). For *S. alba,* RI showed a significant reduction at 60 min of treatment followed also by eutrophication of the roots of the plant after 120 min of illumination in the presence of 0.5 g L^{-1} TiO_2 P25 (−8.99 ± 6.52%), while the RI values for *L. sativum* demonstrated eutrophication at 60 min of treatment, a phenomenon which weakened at the end of the process (−2.54 ± 1.56%). Eutrophication may be attributed to the synergistic effect of bentazon degradation and the formation of inorganic ions, especially NO_3^-. These findings demonstrate that photocatalysis of bentazon in the presence of 0.5 g L^{-1} TiO_2 P25 may not lead to complete mineralization within 120 min of UV-A illumination, but results to a solution with no phytotoxic effect for the tested plant species. Furthermore, these results are in agree-

ment with those of the ecotoxicity evaluation already presented in Section 3.8.1.

4. Conclusions

Photodegradation and mineralization of the herbicide bentazon in the presence of various semiconducting oxides has been investigated in the present study. Degradation follows pseudo-first order kinetics, with TiO_2 P25 providing the best results among the tested commercial TiO_2. The initial degradation rate sharply increases with increasing the TiO_2 P25 loading, up to 0.5 g L^{-1}, while addition of 100 mg L^{-1} H_2O_2 achieves 2-fold increase of the initial degradation rate. The most favorable pH for the decomposition of the herbicide was 6.0, while degradation rates gradually decrease as photocatalysis takes place in neutral or alkaline pH values. Organic sulfur and nitrogen are only partially converted into inorganic in the presence of 0.5 g L^{-1} TiO_2 P25 presenting almost 13.5% and 28.5% conversion, respectively, within 120 min of illumination.

Employing the high resolving power endorsed by a LIT Orbitrap LC-ESI/MS system, 21 TPs including dimers, hydroxy and/or keto bentazon derivatives, and further oxidized species were identified. To the best of our knowledge this is the first report in which such a great number of intermediates has been detected and described in such structural details during the decomposition of bentazon by an AOP, resulting to the elucidation of novel degradation pathways.

Furthermore, ecotoxicity data based on *V. fisheri* bioluminescence inhibition demonstrated that the higher toxicity of bentazon at the first stages of treatment could be attributed to the formation of more toxic intermediates as well as on synergistic effects between them. Toxicity, however, was completely eliminated within 90 min of irradiation under the investigated conditions.

Finally, phytotoxicity of 20 mg L^{-1} aqueous solutions of bentazon, though not particularly high, is completely removed, in the presence of 0.5 g L^{-1} TiO_2 P25 and UV-A irradiation within 120 min, as demonstrated by the negative rates of root inhibition of three higher plant species.

Our findings suggest that TiO_2 mediated photocatalysis has the potential to provide a sustainable solution in the mineralization and detoxification of wastewater containing pesticides, either alone or in combination with other methods i.e. constructed wetlands, reducing the relevant environmental impact and creating water suitable for reuse applications (e.g. irrigation).

Acknowledgements

The study is implemented within the framework of the research project entitled “A novel method for detoxification and reuse of wastewater containing pesticides by solar photocatalysis and constructed wetlands” (project No: 957) of the Action ARISTEIA of the Operational Program “Education and Lifelong Learning” (Action’s Beneficiary: General Secretariat for Research and Technology) and is co-financed by the European Social Fund (ESF) and the Greek State.

Appendix A. Supplementary data

Supplementary data associated with this article can be found, in the online version, at http://dx.doi.org/10.1016/j.apcatb.2016.06.068.

References

[1] M. Manz, K.D. Wenzel, U. Dietze, G. Schuurmann, Sci. Total Environ. 277 (2001) 187–198.
[2] V. Yusa, M. Millet, C. Coscolla, M. Roca, Anal. Chim. Acta 891 (2015) 15–31.
[3] W. Tu, C. Xu, B. Lu, C. Lin, Y. Wu, W. Liu, Sci. Total Environ. 542 (2016) 876–885.
[4] C. Ventura, M.R.R. Nieto, N. Bourguignon, V. Lux-Lantos, H. Rodriguez, G. Cao, A. Randi, C. Cocca, M. Nunez, J. Steroid Biochem. 156 (2016) 1–9.
[5] G.V.A.A.M. Fan, Off. Environ. Health Hazard Assess. (1999).
[6] J.R. Abernath, L.M. Wax, Weed Sci. 21 (1973) 224–227.
[7] A. Mine, S. Matsunaka, Pestic. Biochem. Phys. 5 (1975) 444–450.
[8] S. Chiron, E. Martinez, D. Barcelo, J. Chromatogr. A 665 (1994) 283–293.
[9] G.M.F. Pinto, I.C.S.F. Jardim, J. Chromatogr. A 846 (1999) 369–374.
[10] WHO, WHO Guidelines for Drinking Water Quality, Geneva (2004).
[11] WHO, The WHO recommended classification of pesticides by hazard and guidelines to classification 2009, Geneva (2009).
[12] J. Neuschl, P. Kacmar, Vet. Med. Czech 38 (1993) 115–121.
[13] A. Turcant, P. Harry, A. Cailleux, M. Puech, C. Bruhat, N. Vicq, A. Le Bouil, P. Allain, J. Anal. Toxicol. 27 (2003) 113–117.
[14] I.W. Wu, M.S. Wu, J.L. Lin, J. Nephrol. 21 (2008) 256–260.
[15] M. Kock-Schulmeyer, M. Villagrasa, M.L. de Alda, R. Cespedes-Sanchez, F. Ventura, D. Barcelo, Sci. Total Environ. 458 (2013) 466–476.
[16] A. Derbalah, A. Ismail, A. Hamza, S. Shaheen, Water Environ. Res. 86 (2014) 584–593.
[17] V. Kitsiou, N. Filippidis, D. Mantzavinos, I. Pouios, Appl. Catal. B Environ. 86 (2009) 27–35.
[18] I.K. Konstantinou, T.A. Albanis, Appl. Catal. B Environ. 42 (2003) 319–335.
[19] B. Toepfer, A. Gora, G. Li Puma, Appl. Catal. B Environ. 68 (2006) 171–180.
[20] N.A. Mir, M.M. Haque, A. Khan, M. Muneer, S. Vijayalakshmi, Environ. Technol. 35 (2014) 407–415.
[21] E. Pelizzetti, V. Maurino, C. Minero, O. Zerbinati, E. Borgarello, Chemosphere 18 (1989) 1437–1445.
[22] C. Berberidou, V. Kitsiou, S. Karahanidou, D.A. Lambropoulou, A. Kouras, C.I. Kosma, T.A. Albanis, I. Poulios, J. Chem. Technol. Biotechnol. (2015), http://dx.doi.org/10.1002/jctb.4848 (Article in press).
[23] A.M. Braun, M.T. Maurette, E. Oliveros, Photochemical Technology, Wiley, New York, 1991.
[24] J.B. Baxter, C.A. Schmuttenmaer, J. Phys. Chem. B 110 (2006) 25229–25239.
[25] E.A. Meulenkamp, J. Phys. Chem. B 103 (1999) 7831–7838.
[26] M. Kositzi, I. Poulios, K. Samara, E. Tsatsaroni, E. Darakas, J. Hazard. Mater. 146 (2007) 680–685.
[27] P. Spathis, I. Poulios, Corros. Sci. 37 (1995) 673–680.
[28] K.L.E. Kaiser, V.S. Palabrica, Water Qual. Res. J. Can. 26 (1991) 361.
[29] D.C. Hurum, A.G. Agrios, K.A. Gray, T. Rajh, M.C. Thurnauer, J. Phys. Chem. B 107 (2003) 4545–4549.
[30] T. Fotiou, T.M. Triantis, T. Kaloudis, A. Hiskia, Chem. Eng. J. 261 (2015) 17–26.
[31] T. Fotiou, T.M. Triantis, T. Kaloudis, K.E. O'Shea, D.D. Dionysiou, A. Hiskia, Water Res. 90 (2016) 52–61.
[32] S. Goldstein, D. Behar, J. Rabani, J. Phys. Chem. C 112 (2008) 15134–15139.
[33] J.A. Rengifo-Herrera, K. Pierzchala, A. Sienkiewicz, L. Forro, J. Kiwi, C. Pulgarin, Appl. Catal. B Environ. 88 (2009) 398–406.
[34] J.A. Rengifo-Herrera, C. Pulgarin, Sol. Energy 84 (2010) 37–43.
[35] S. Parra, J. Olivero, C. Pulgarin, Appl. Catal. B Environ. 36 (2002) 75–85.
[36] D. Robert, B. Dongui, J.V. Weber, J. Photochem. Photobiol. A 156 (2003) 195–200.
[37] H. Alekabi, N. Serpone, J. Phys. Chem. 92 (1988) 5726–5731.
[38] G.J. Cunningham, S. Al-Sayyed, S. Srijaranai, Adsorption of model pollutants onto TiO_2 particles in relation to photoremediation of contaminated water, in: G. Heltz, R. Zepp, D. Crosby (Eds.), Aquatic and Surface Photochemistry, Lewis Publishers, CRC Press, 1994, pp. 317–348 (Chapter 22).
[39] S. Helali, F. Dappozze, S. Horikoshi, T.H. Bui, N. Perol, C. Guillard, J. Photochem. Photobiol. A 255 (2013) 50–57.
[40] N. Philippidis, S. Sotiropoulos, A. Efstathiou, I. Poulios, J. Photochem. Photobiol. A 204 (2009) 129–136.
[41] B. Zielinska, J. Grzechulska, R.J. Kalenczuk, A.W. Morawski, Appl. Catal. B Environ. 45 (2003) 293–300.
[42] C. Tizaoui, K. Mezughi, R. Bickley, Desalination 273 (2011) 197–204.
[43] C.O. Ania, F. Beguin, Water Res. 41 (2007) 3372–3380.
[44] M.M. Halmann, Photodegradation of Water Pollutants, CRC Press, Boca Raton, 1996.
[45] S. Malato, J. Blanco, M.I. Maldonado, P. Fernandez-Ibanez, A. Campos, Appl. Catal. B Environ. 28 (2000) 163–174.
[46] A.J. Hoffman, E.R. Carraway, M.R. Hoffmann, Environ. Sci. Technol. 28 (1994) 776–785.
[47] C. Kormann, D.W. Bahnemann, M.R. Hoffmann, Environ. Sci. Technol. 22 (1988) 798–806.
[48] S. Kaniou, K. Pitarakis, I. Barlagianni, I. Poulios, Chemosphere 60 (2005) 372–380.
[49] T. Velegraki, E. Hapeshi, D. Fatta-Kassinos, I. Poulios, Appl. Catal. B Environ. 178 (2015) 2–11.
[50] L.A. Ioannou, E. Hapeshi, M.I. Vasquez, D. Mantzavinos, D. Fatta-Kassinos, Sol. Energy 85 (2011) 1915–1926.
[51] D.D. Dionysiou, M.T. Suidan, I. Baudin, J.M. Laine, Appl. Catal. B Environ. 50 (2004) 259–269.
[52] S. Goldstein, D. Behar, J. Rabani, J. Phys. Chem. C 113 (2009) 12489–12494.
[53] A.G. Rincon, C. Pulgarin, Catal. Today 124 (2007) 204–214.
[54] M.S. Nahar, K. Hasegawa, S. Kagaya, S. Kuroda, J. Hazard. Mater. 162 (2009) 351–355.
[55] H. Mestankova, G. Mailhot, J. Jirkovsky, J. Krysa, M. Bolte, Environ. Chem. Lett. 7 (2009) 127–132.
[56] T. Ohno, D. Haga, K. Fujihara, K. Kaizaki, M. Matsumura, J. Phys. Chem. B 101 (1997) 6415–6419.

[57] S.W. Lam, K. Chiang, T.M. Lim, R. Amal, G.K.C. Low, J. Catal. 234 (2005) 292–299.
[58] M. Mrowetz, E. Selli, J. Photochem. Photobiol. A 162 (2004) 89–95.
[59] H. Mestankova, J. Krysa, J. Jirkovsky, G. Mailhot, M. Bolte, Appl. Catal. B Environ. 58 (2005) 185–191.
[60] U. Cernigoj, U.L. Stangar, J. Jirkovsky, J. Hazard. Mater. 177 (2010) 399–406.
[61] A. Aguera, L.A.P. Estrada, I. Ferrer, E.M. Thurman, S. Malato, A.R. Fernandez-Alba, J. Mass Spectrom. 40 (2005) 908–915.
[62] I.K. Konstantinou, D.A. Lambropoulou, T.A. Albanis, Xenobiotics in the Urban Water Cycle: Mass Flows, Environmental Processes, Mitigation and Treatment Strategies—Environmental Pollution, Springer, Netherlands, 2010.
[63] M. Davezza, D. Fabbri, E. Pramauro, A.B. Prevot, Chemosphere 86 (2012) 335–340.
[64] B. Eyheraguibel, A. ter Halle, C. Richard, J. Agric. Food Chem. 57 (2009) 1960–1966.
[65] M. Peschka, M. Petrovic, T.P. Knepper, D. Barcelo, Anal. Bioanal. Chem. 388 (2007) 1227–1234.
[66] E.I. Seck, J.M. Dona-Rodriguez, C. Fernandez-Rodriguez, O.M. Gonzalez-Diaz, J. Arana, J. Perez-Pena, Chem. Eng. J. 203 (2012) 52–62.
[67] W.R. Knauber, A.J. Krotzky, B. Schink, Environ. Sci. Technol. 34 (2000) 598–603.
[68] K.I. Antonopoulou, Appl. Catal. A Gen. 515 (2016) 136–143.